Journal of Alloys and Compounds 1022 (2025) 180013

Contents lists available at ScienceDirect

Journal of Alloys and Compounds

journal homepage: www.elsevier.com/locate/jalcom

The origin of magneto-structural coupling in Fe-based bulk metallic glasses

Alexander Firlus [a,*], Mihai Stoica [a], Jonathan Wright [b], Xiao Sun [c], Robin E. Schäublin [a], Jörg F. Löffler [a,*]

[a] Laboratory of Metal Physics and Technology, Department of Materials, ETH Zurich, 8093 Zurich, Switzerland
[b] European Synchrotron Radiation Facility (ESRF), Avenue des Martyrs 71, 38043 Grenoble, France
[c] Deutsches Elektronen-Synchrotron (DESY), Notkestrasse 85, 22607 Hamburg, Germany

ARTICLE INFO

Keywords:
Bulk metallic glasses
Invar effect
Magnetism
Amorphous alloys
Iron
Synchrotron radiation

ABSTRACT

All ferromagnetic Fe-based bulk metallic glasses show the Invar effect. It is a magnetic effect that reduces the coefficient of thermal expansion and comes in two forms, a step-type and a peak-type effect. Here, we study the atomic arrangement of an $(Fe_{71.2}B_{24}Y_{4.8})_{96}Nb_4$ bulk metallic glass as a function of temperature and across more than six orders of magnitude in length scale. Combining various synchrotron-based X-ray scattering techniques we show that the Invar effect originates at the atomic scale within the Fe–Fe network. We find no signs of increased spatial correlations due to the ferromagnetic interactions. This shows that no structural rearrangement occurs at the Curie temperature and that the Invar effect is purely of energetic nature. We conclude that the Invar effect has a fundamental base that results from the magnetic interactions of Fe–Fe bonds. Based on this, we provide a model for the magnetic interactions that create the Invar effect in amorphous materials.

1. Introduction

The Invar effect, an anomalously low coefficient of thermal expansion (CTE), $\alpha = \frac{1}{L}\frac{dL}{dT}$, caused by magnetic interactions was first observed in 1896 by Guillaume [1,2] in crystalline 65Fe35Ni, the classical Invar alloy. While there are many approaches to design a material with a low or zero CTE, the Invar effect relies on ferromagnetic interactions and thus it vanishes at the Curie temperature T_C. This gives rise to an abrupt change in the CTE at T_C. Despite this effect being known for over a century, there is still no complete and conclusive description of its atomic origins. Thermal expansion is linked to the asymmetry of the interatomic potential, but in materials showing the Invar effect there is an additional contribution to the CTE, resulting in $\alpha = \alpha_{asym} + \alpha_{anom}$, where the anomalous component α_{anom} is of opposite sign to α_{asym}. All explanations on the Invar effect agree that α_{anom} originates from the magnetic properties of the material. However, the exact origin is still debated, and surprisingly, considering that the magnetic energy per atom is typically a few meV, it is insignificant compared to the binding energy between atoms (a few eV). Nevertheless, magnetic interactions at the atomic scale are very sensitive to the local atomic arrangement. Therefore, the gradients with respect to spatial variations (for example, changes in bond distances or bond angles) can be large.

α_{asym} is associated with phonon-phonon interactions, i.e. vibrations in the atomic arrangement. Lohaus et al. recently provided experimental evidence that α_{anom} in the classical Invar alloy originates from the entropy in the spin system [3]. Through spin-phonon interactions the phonon density of states is stabilized. This helps to maintain the spin and phonon contributions to the CTE at equal magnitude but with opposite sign, effectively canceling each other.

Ab-initio calculations on the classical Invar alloy attributed the anomalous magneto-volume coupling to the magnetic interaction of neighboring Fe–Fe pairs, whereas Ni does not show any anomalies [4]. In general, the Invar effect is rare in crystalline alloys, and even within the binary Fe–Ni system only stoichiometries close to 65 wt% Fe show the Invar effect [1]. In contrast, the Invar effect is universally seen in magnetic Fe-based bulk metallic glasses (BMGs) [5]. However, the lack of long-range order (LRO) in BMGs makes it difficult to transfer the results obtained from modeling the crystalline Invar alloys to amorphous Invar alloys. In fact, differences between crystalline and amorphous alloys with the Invar effect are so big that there may be a different physical mechanism behind it as we will present here. Besides the structural differences, also the electronic structure of Fe-based BMGs is very different. All crystalline Invar alloys have a similar electron concentration of around 8.6 electrons/atom [6,7], while those of Fe-based BMGs range from 6.5 to 7.1 electrons/atom, i.e. it is much lower and spans a much larger range.

* Corresponding authors.
E-mail addresses: alexander.firlus@mat.ethz.ch (A. Firlus), joerg.loeffler@mat.ethz.ch (J.F. Löffler).

https://doi.org/10.1016/j.jallcom.2025.180013
Received 22 October 2024; Received in revised form 13 February 2025; Accepted 24 March 2025
Available online 25 March 2025

The situation is complicated even more by the observation that BMGs can show two kinds of Invar effect, a step-like increase of the CTE at the Curie temperature and a peak-like reduction of the CTE only around T_C. It is therefore possible that the magnetic interactions either reduce the CTE at all temperatures below T_C (step-type) or only at T_C (peak-type) [5]. These two types are not unique features of BMGs but also crystalline alloys can show both types [8]. Which of these two appears seems to depend on the magnetic properties only, in particular the saturation magnetization and Curie temperature.

Still, all studied BMGs confirm the existence of the Invar effect through macroscopic dilatometry. Recently, we could also experimentally verify that the Invar effect in amorphous materials originates at the atomic scale from Fe–Fe pairs and that other alloying elements do not contribute directly [9,10]. This is also supported by prior observations, where Fe–B- and Fe–P-based bulk metallic glasses all exhibit the Invar effect [11]. The Invar effect is associated with the local atomic arrangement and a high Fe concentration [5] is needed to obtain a highly-coordinated Fe network. However, this still leaves the influence of the Invar effect on intermediate length scales (above 1 nm and below 1 mm) unexplored. This length scale is, however, relevant because magnetic interactions can be of long-range, and magnetic structures such as domain walls or long-range magnetostatic interactions fall outside the previously studied experimental windows. These considerations are particularly relevant in disordered materials such as BMGs as their disordered atomic arrangement will influence the long-range order magnetic structure. It is therefore important to understand how the magnetic interactions affect the structure at length scales in between the atomic and macroscopic scale, because these may give insights into what type of magnetic interactions and conditions are responsible or required for the Invar effect to occur.

It was shown recently that it is solely Fe that actively enables and controls the Invar effect [10]. It is therefore of interest to study the features of the Fe network at all length scales in particular whether the magnetic LRO (such as ferromagnetic spin alignment) modifies the atomic arrangement. We address this challenge by studying the correlation functions at all length scales as a function of temperature and in particular compare the ferromagnetic to the paramagnetic state.

In this study, we investigate the Invar effect in the quaternary $(Fe_{71.2}B_{24}Y_{4.8})_{96}Nb_4$ (denoted here QNb) bulk metallic glass [12,13]. Several in-situ X-ray-based techniques were employed to study the atomic arrangement at all length scales. XRD provides information at the atomic scale that helped us to unveil the atomic origin of the Invar effect [9]. However, this technique is limited to length scales up to around 1 nm. At intermediate length scales, small-angle X-ray scattering (SAXS) is more adequate, as it reveals correlations at length scales of up to a few hundreds of nanometers. At even larger length scales, spatially-resolved X-ray diffraction computed nanotomography (XRD-nCT) was performed. Based on the experimental observations, we present a refined model for the occurrence of the two types of Invar effect in BMGs.

2. Methods

2.1. Sample preparation

The (FeBY)Nb master alloys were prepared from pure elements with purities of 99.5 % for B and 99.97 % for Fe. Nb was included in the master alloy via an 25Fe75Nb pre-alloy made from 99.95 % pure Nb (and 99.97 % pure Fe). The elements were alloyed through arc melting in a Ti-gettered (99.999 % pure) argon atmosphere. The resulting button was flipped over and remelted several times to ensure homogeneity. Arc melting a piece from the master alloy and pulling the melt into a water-cooled copper mold produced rods of 3 mm in diameter. Thin disks were cut for further experiments.

2.2. X-ray diffraction computed nanotomography

The X-ray diffraction computed nanotomography experiments were performed at ESRF, beamline ID11 at experimental hall 3, using a 500 nm × 500 nm monochromatic beam at 64.58 keV. The diffraction patterns were recorded with a DECTRIS EIGER2 X CdTe 4 M detector at 0.1 s exposure time per frame. The exact beam energy and sample-to-detector distance were calibrated with a CeO_2 standard sample.

For the tomography the rotational scan was performed at every 1° for a total of 180°. At each rotation a line scan of 160 points each spaced 500 nm apart was recorded. The temperature control was achieved by a home-made heating stage. With this setup the theoretical resolution of the reconstruction is 500 nm and connects to the length scales studied with SAXS.

The sample itself was a fragment that was cut from the QNb bulk metallic glass. Due to the thermal expansion of the sample holder the reconstructed slices differ from each other but are from the same fragment. Details on the reconstruction can be found in the Supplemental Material.

2.3. In-situ small-angle/wide-angle X-ray scattering

The small-angle X-ray scattering experiments were performed at DESY, beamline P62 [14], with a 1 mm × 1 mm monochromatic beam of 29 keV. The scattering images were recorded on a DECTRIS EIGER2 9 M detector (placed in vacuum) at roughly 3500 mm sample-to-detector distance with 20 s exposure time per frame. The parameters of the setup were chosen such that it covers the range between the atomic-scale XRD experiments and the XRD-nCT. The exact beam energy and sample-to-detector distance were calibrated with a silver behenate (AgBh) standard sample. The absolute units of the scattering cross section were determined by calibration with a glassy carbon reference sample, taking the sample thickness and absorption into account.

The wide-angle X-ray scattering was performed in parallel with the SAXS. The diffraction patterns were recorded on a DECTRIS EIGER2 4 M detector at around 126 mm sample-to-detector distance. The exact geometry of the setup was calibrated with a Si powder reference sample.

3. Results

3.1. The origins of the Invar effect

The Curie temperature is around 500 K for QNb and it also coincides with the dilatometric transition temperature at which the CTE increases [9,12,13,15,16]. Fig. 1 shows the wide-angle X-ray scattering (WAXS) profile of QNb. The room-temperature WAXS scattering profile of QNb (see Fig. 1a) confirms the amorphous state of the alloy. We have shown that both the first and the second diffraction peaks accurately reflect the thermal expansion at the atomic scale [9]. The change in the second peak position q_2 as a function of temperature is shown in Fig. 1b. There is a distinct change in slope at the Curie temperature of around 500 K. This is evidence for the existence of the atomic-scale Invar effect in this sample.

3.2. SAXS

SAXS allows investigating the scattering of X-rays at small q values close to the primary beam. It is therefore sensitive to correlations at larger length scales. We have shown that the Invar effect provides evidence that the magnetic interactions in Fe-based BMGs are sufficiently strong to affect the atomic structure [9]. This raises the question of whether the ferromagnetic order will also encourage a (partial) ordering of the atomic arrangement and thus introduce long-range correlations. Fig. 2a shows the SAXS intensity profile of QNb during the thermal treatments. It was measured simultaneously to WAXS. The white line in the color coding serves as an isoline. The scattering profiles have no

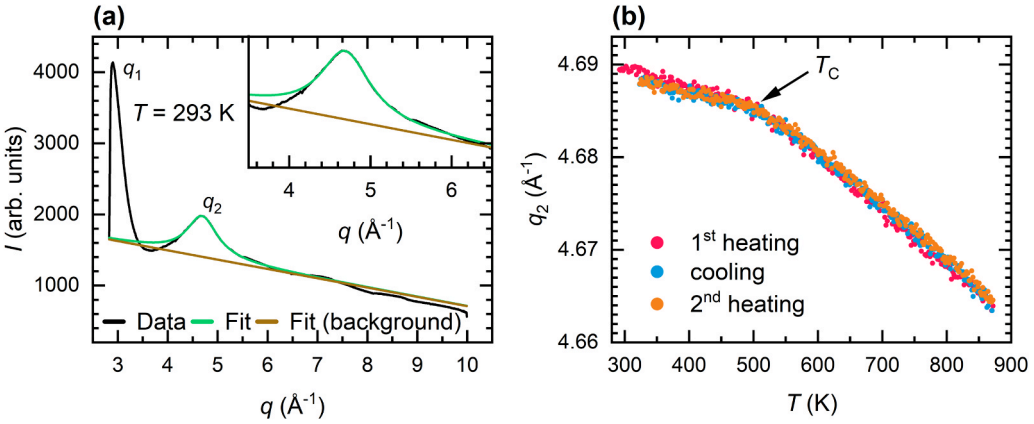

Fig. 1. WAXS intensity profile and atomic-scale thermal expansion of QNb. **(a)** The WAXS profile of QNb at room temperature shows several broad diffraction peaks. A Lorentzian fit (with linear background) is shown as well. The inset presents a magnified view of the fitted peak. **(b)** The average peak position as a function of temperature is piecewise linear with a breaking point at the Curie temperature (around 500 K).

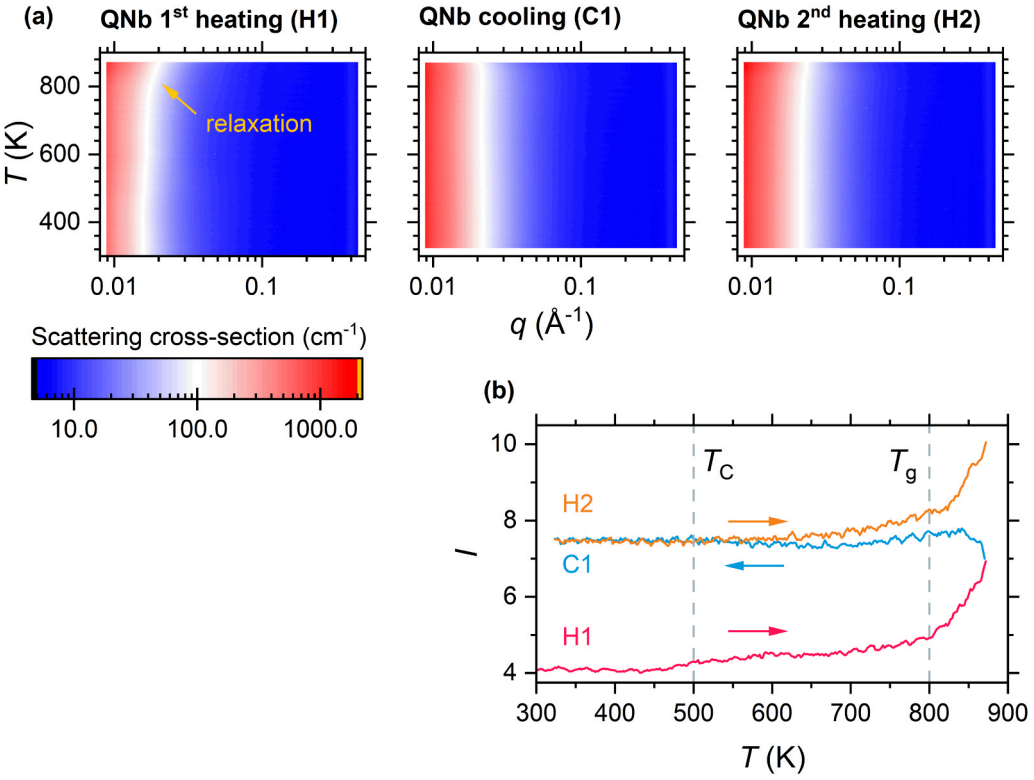

Fig. 2. SAXS intensity of QNb as a function of temperature. **(a)** There are no peaks, which indicates that no clustering occurs in these glasses. There is no change in the intensity profiles at the Curie temperature (around 500 K). At temperatures up to the glass transition temperature (≈ 800 K) free volume is annihilated (relaxation) and thus the intensity increases at all q values. **(b)** The integrated intensity profile confirms the structural rearrangement at the glass transition temperature. There is no rearrangement at the Curie temperature.

peaks, which is a clear sign for the absence of long-range ordering at scales of up to 100 – 200 nm. Up to the glass transition temperature (≈ 800 K) the signal intensity is increased at all q values, which indicates relaxation of the glassy state and the irreversible reduction of free volume. This effect is particularly strong in the as-cast samples, i.e. during the first heating segment. Thus, SAXS is sensitive enough to resolve the glass transition at which the CTE of bulk metallic glasses tends to double [17,18]. However, there is no effect on the scattering intensity at the Curie temperature (around 500 K) despite the change in the CTE by a factor of 3 – 5. Fig. 2b shows the integrated scattering intensity in the range $q < 0.3$ Å^{-1} as a function of temperature. It quantifies and validates the absence of structural rearrangement at T_C. It can therefore be concluded that the magnetic interactions do not encourage any long-range (partial) ordering of the atomic arrangement and the increase in the CTE at T_C is due to a different mechanism than that at T_g.

3.3. XRD tomography

After having proven that the magnetic interactions do not impose structural ordering, the question about magnetic structures and their influence has been investigated. They can be many micrometers in size. In-situ nCT-XRD provides access to this length scale and has been used to study the spatial distribution of atomic arrangements [19]. It is a powerful technique as the full diffraction pattern is recorded for each

point in the projection. Therefore, multiple metrics can be compared for the same volume. Compared to XRD/WAXS a large number of diffraction patterns is combined for the reconstruction. Before using nCT-XRD to investigate spatial correlations related to the Invar effect (or their absence) it is of value to confirm that the data is of sufficient quality to reveal the Invar effect. Fig. 3 shows the distribution of the position of the first diffraction peak at various temperatures. Fig. 3a shows a shift of the diffraction peak to smaller q values as temperature increases. This trend is expected for thermal expansion. However, in alloys with the Invar effect, the rate of change is low at temperatures below T_C and increases by up to one order in magnitude at T_C. Fitting a Lorentzian peak function to the histograms reveals the average peak position $\langle q_{peak} \rangle$ as a function of temperature. Fig. 3b shows the change in thermal expansion at the Curie temperature of QNb. Just like the WAXS datasets (see Fig. 1), the central peak position reveals the Invar effect. Therefore, nCT-XRD is precise enough to resolve it. However, given the acquisition time of more than 30 min per scan the number of data points is much less than in the in-situ WAXS experiments (cf. Fig. 1). Consequently, the Curie temperature can only be determined qualitatively as deviation from the high-temperature linear fit (green line).

Following that observation, the spatial correlations are studied via the reconstruction of the nCT-XRD projections. Fig. 4 shows the reconstruction of slices in the QNb fragments at various temperatures. The top rows show the reconstruction according to the height of the first diffraction peak. This metric measures the density (and thickness) and proves the chemical homogeneity and amorphicity of the studied samples. The reconstructions according to strain (i.e. related to the central position q_1 of the first sharp diffraction peak) can be found below. This metric is a measure of the average short-range order. The procedure is explained in [20,21]. No spatial variation of the average q_1 is found within the sample, neither below the Curie temperature nor above it. Thus, no atomic rearrangement or partial ordering at the micrometer scale is observed. We thus conclude that the Invar effect is homogeneously distributed throughout the sample.

In summary, the Invar effect can be seen at the atomic scale in the average bond distances, especially Fe−Fe. The temperature-induced changes are fully reversible around T_C [9] and other elements do not seem to play an active role in the Invar effect [10]. Beyond the SRO, no structural variations nor partial ordering is observed at longer length-scales. We thus can conclusively summarize that the Invar effect originates at the atomic scale from the magnetic interactions of the Fe network. It causes a strong anomalous contribution to the thermal expansion that is opposite in sign to the thermal expansion due to the asymmetry of the pair potential. Despite the fact that the magnetic interactions are strong enough to cause a net-negative thermal expansion between neighboring Fe–Fe pairs [9], they do not promote any structural rearrangement at any length scale.

4. Discussion

Many unique properties of bulk metallic glasses, such as their high hardness, high strength, high elastic limit, and low magnetic anisotropy of Fe-based glasses, could already be explained at the atomic scale. The mechanism behind the universal Invar effect in amorphous alloys has not yet been resolved. In the following we provide an atomic-scale model based on the experimental results of this study.

Investigations of the pair distribution function revealed that the magnetic interactions can even cause a negative thermal expansion in Fe-based BMGs [9]. This implies that their influence on the disordered local atomic arrangement is of equal importance as structural/chemical effects. Here, we find that the magnetism is nevertheless not promoting any spatial correlations. Consequently, the bridging of the Invar effect from the atomic to the macroscopic scale is within the disordered network of Fe atoms. It follows that there needs to be a cluster of Fe atoms that extends through the whole sample. This suggests that the Invar effect (at macroscopic scale) is only possible in Fe-based BMGs with an Fe concentration that is high enough to guarantee that each Fe atom is sufficiently bonded to many other Fe atoms. In combination with the two-networks model we developed [10], the effect of Co and Ni can be understood as well. Both elements are known to severely reduce the anomalous component in the thermal expansion, i.e. reduce the strength of the Invar effect. Since their atomic size is similar to that of Fe (rather than e.g. B, Y, Nb), these atomic species are preferentially substituting Fe. Even a small addition of Ni or Co can split the spanning Fe cluster into multiple smaller ones. The anomalous thermal expansion within these smaller clusters is then compensated by the boundary regions, which negates (to a large degree) the Invar effect at the macroscopic scale. Therefore, Fe−Fe pairs in Fe−Ni/Co-based BMGs may experience the atomic-scale Invar effect but it does not scale up to macroscopic scales in those alloys.

Besides the lack of long-range structural correlations caused by magnetic interactions, the Invar effect is also spatially homogeneous at intermediate length scales. The XRD-nCT shows no spatial variations in the bond distances. It can therefore be concluded that the anomalous contribution to the thermal expansion α_{anom} arises only from the magnetic interaction of Fe–Fe pairs (and possibly also more distant Fe atoms) and is transmitted to the macroscopic scale via the sample-spanning Fe

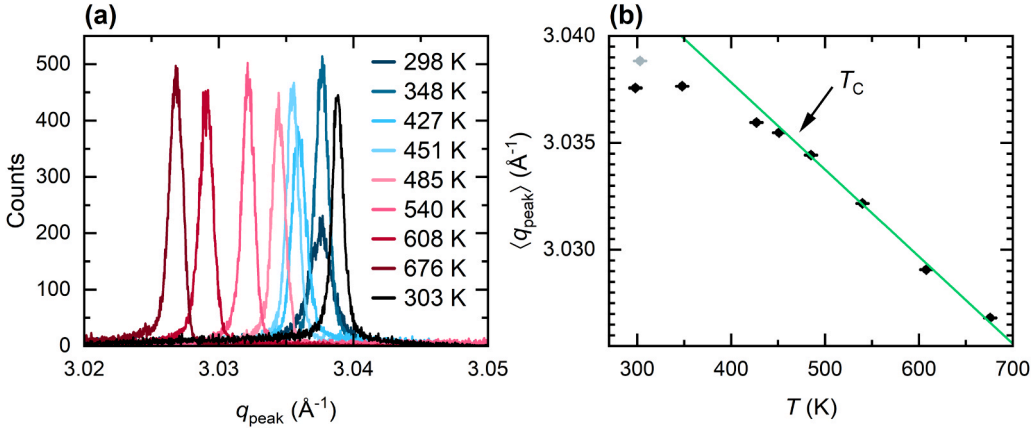

Fig. 3. Distribution of the first diffraction peak center of QNb as a function of temperature. **(a)** The histograms of the first diffraction peak position of QNb show a shift to smaller q values at increased temperatures. The black line (303 K) represents the condition after thermal cycling. **(b)** The histograms were fitted with a Lorentzian peak function and the temperature influence on the diffraction peak position of QNb shows a reduced thermal expansion below T_C. The error bars represent three standard deviations of the fitting parameter. The condition after thermal cycling is highlighted in grey. The green line represents a linear fit to the high-temperature thermal expansion and the deviation of the data from this line indicates the Curie temperature.

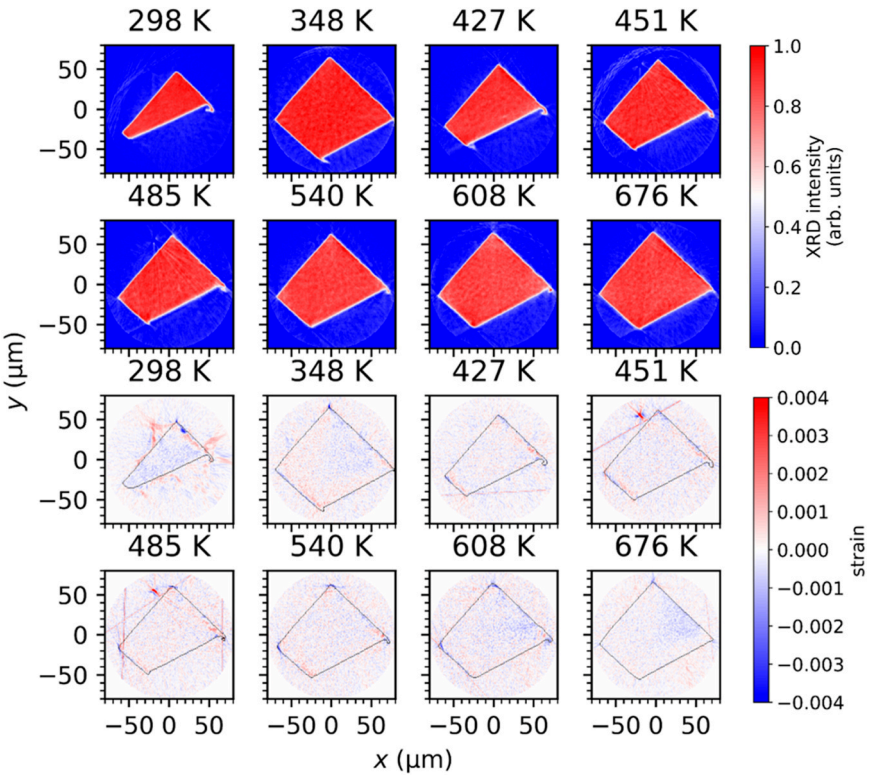

Fig. 4. nCT-XRD reconstruction of slices of QNb at multiple temperatures. The reconstruction according to the height of the first diffraction peak (top rows) reproduces the shape of the sample and shows only slight density (and thickness) variations of less than 4 %. Reconstruction via strain (bottom rows) yields no spatial variation above 500 nm length scale. The sample outline is highlighted by black lines.

network. From the present length-scale investigation, it is clear that the Invar effect in BMGs is not an emergent property (i.e. resulting from a specific atomic arrangement) but rather results directly from the atomic-scale magnetic interactions.

These insights make it possible to understand the Invar effect at the atomic level, in particular the continuous transition from the step-type Invar effect, in which the CTE is reduced at all temperatures below the Curie temperature, to the peak-type Invar effect, which shows a reduced CTE only around the Curie temperature [5]. The two types are not separated by the alloys' chemical composition but rather by their magnetic properties, the Curie temperature and the saturation magnetization. Even within a given alloy series the transition from a step-like to a peak-like Invar effect is possible, as was shown for $Fe_{76-x}Si_{3.3}P_{8.7}C_7B_5Mo_x$ ($x = 0$–5) BMGs [5]. A step-like Invar effect is associated with a low Curie temperature and low saturation magnetization (typically less than 300 °C and less than 1.1 T, respectively), while the peak-like Invar effect is observed in BMGs with a high Curie temperature and high saturation magnetization [5]. Moreover, neither the Curie

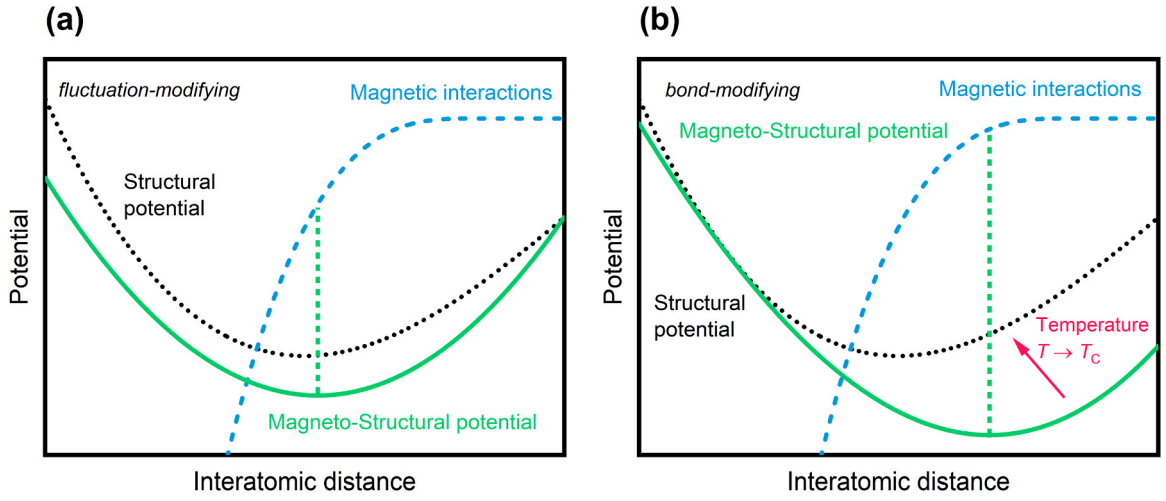

Fig. 5. Sketch of the mechanism behind the two types of Invar effect. In the absence of magnetic interactions only the local atomic structure determines the interatomic potential (black dotted line). **(a)** If the magnetic interactions are weak, the equilibrium distance does not change much but further expansion requires an additional energy contribution. This leads to a significantly reduced CTE below T_C. **(b)** If the magnetic interactions are strong, the equilibrium distance is strongly affected by them. At the new equilibrium further expansion requires only little energy but at the Curie temperature the equilibrium distance shifts back to its structural equilibrium and thus causes a reduced CTE at T_C.

temperature nor the saturation magnetization alone are able to separate the two types of Invar effect. Instead, the combination of both is required.

Based on X-ray diffraction data [9,10] and this study it is clear that the magnetic contribution to thermal expansion originates from the atomic scale as well. The magnetic exchange energy H_{mag} can be described in the Heisenberg model as $H_{\mathrm{mag}} = -\frac{1}{2}\sum_{i,j} J_{ij}\,\mathbf{m}_i \cdot \boldsymbol{m}_j$, where J_{ij} is the exchange coupling between sites (i.e. Fe atoms) i and j, and $\mathbf{m}_i$ is the magnetic moment at site i. Oftentimes, only the interactions between nearest neighbors are considered. Macroscopically, the Curie temperature scales with the average exchange coupling and the saturation magnetization is proportional to the average magnetic moment. In this light, it is the magnetic energy that determines which type of Invar effect will be observed.

Fig. 5 helps to understand the mechanism behind the two types of Invar effect and is explained in the following. In amorphous materials there is a wide range of interatomic distances. It is rather unlikely that the structural bonding preferences coincide with the magnetic preferences that arise from the distance dependence of J_{ij} and $|\mathbf{m}|$. It has been shown that the relationship of the magnetic moment per atom with distance has a negative curvature in all bcc metals, i.e. increases sharply at small distances and becomes flat towards large distances [22]. It is therefore reasonable to expect that also the magnetic potential H_{mag} has a similar shape in amorphous metals. When the contribution of H_{mag} to the total energy is small (relative to the configurational energy), the atomic arrangement is only slightly modified by the magnetic interactions, as illustrated in Fig. 5a. The magnetic interactions are, however, able to generate a more symmetric magneto-structural potential, as is illustrated by the green solid curve in Fig. 5a. Here, the magnetic contribution to the thermal expansion will be high, because $\frac{\mathrm{d}H_{\mathrm{mag}}}{\mathrm{d}r}$ is high at the interatomic distance where the system is in equilibrium (minimum of the magneto-structural potential), which is far away from the magnetic equilibrium (dashed blue curve). This magnetic contribution will not change much as a function of temperature as the thermal expansion will only slightly change the bond lengths and the average bond distance always stays in the steep part of the magnetic interactions. At the Curie temperature, however, the correlation between neighboring magnetic moments will be lost ($\langle \mathbf{m}_i \cdot \mathbf{m}_j \rangle = 0$) such that the gradient of H_{mag} becomes irrelevant. This results in a step-like increase of the CTE at the Curie temperature.

On the other hand, if H_{mag} provides a significant contribution to the total energy, then the bond distances will be modified towards the magnetic equilibrium. As a consequence, $\frac{\mathrm{d}H_{\mathrm{mag}}}{\mathrm{d}r}$ at the new total-energy equilibrium (minimum of the solid green curve in Fig. 5b) is small and the CTE will not be reduced by the magnetic contribution. Instead, as the temperature approaches the Curie temperature, the magnetic system becomes progressively more disordered and consequently H_{mag} becomes less relevant in determining the bond distances. Therefore, the equilibrium bond distances shift back to the one preferred by the atomic structure (see arrow in Fig. 5b), which results in a peak-like reduction of the CTE at or just before the Curie temperature.

The two types of Invar effect can therefore be differentiated by the relative magnitude of the magnetic potential energy H_{mag} compared to the structural one. Weak magnetic properties are fluctuation-modifying and cause the step-type Invar effect by making the total interatomic potential more symmetric below T_{C}, while strong magnetic interactions are bond-modifying and thus cause the peak-type Invar effect by shifting the equilibrium position below T_{C}.

In this model, unlike the phenomenological explanation proposed in [5], it is not one specific atomic distance of Fe–Fe pairs that contributes to the Invar effect but rather all Fe atoms. The atomic structure of Fe-based BMGs is best viewed as two interwoven networks, the Fe network and the backbone network [10,23,24]. In the absence of LRO the competition between the magnetic and structural interactions will be optimized locally. Stresses that may build up due to element-selective (here Fe) reduced thermal expansion can be accommodated in the backbone network and the related free volume. In contrast, the minimization of the potential energy has to occur globally in crystalline alloys. The Invar effect is thus rarely seen in crystalline materials but occurs universally in Fe-based BMGs.

5. Conclusions

The anomalously low CTE of Fe-based BMGs is called Invar effect in analogy to the one of the FeNi Invar alloy. It is a magnetic effect and comes in two forms, a continuously reduced CTE at all temperatures below T_{C} (step-type Invar effect) and a reduction of the CTE just at T_{C} (peak-type Invar effect). Synchrotron-based X-ray scattering techniques have been used to investigate the length scales of the magnetic contribution to the thermal expansion in BMGs. While WAXS confirms the existence of the Invar effect at the atomic scale, SAXS experiments show no correlation between the atomic arrangement and the structure at the nano- to micrometer scale. Moreover, nCT-XRD also proves that the structure is homogeneous at the micrometer scale and not correlated to any SRO or MRO.

Based on this, it can be concluded that the origin of the Invar effect is in the magnetic interactions at the atomic scale. It is a fundamental phenomenon and does not emerge from a complex atomic arrangement. All Fe atoms can contribute to it. With these insights, the magnetic interactions responsible for the two types of Invar effect can be understood as fluctuation-modifying and bond-modifying. The universality of the Invar effect in BMGs comes from the disordered atomic arrangement (absence of LRO), which allows to accommodate some stress and enable a local potential energy optimization. This is different to crystalline alloys, which have an ordered atomic structure and thus require a global response to the competition between the magnetic and structural interactions. This opens the door for tailoring the Invar property of bulk metallic glasses during casting or post-processing, for example by heat treatment.

CRediT authorship contribution statement

Löffler Jörg F.: Writing – review & editing, Validation, Supervision, Project administration, Methodology, Funding acquisition, Conceptualization. **Schäublin Robin E.:** Writing – review & editing, Validation, Methodology. **Sun Xiao:** Writing – review & editing, Validation, Investigation, Data curation. **Wright Jonathan:** Writing – review & editing, Visualization, Validation, Software, Investigation, Formal analysis, Data curation. **Stoica Mihai:** Writing – review & editing, Writing – original draft, Validation, Project administration, Methodology, Investigation, Formal analysis, Conceptualization. **Firlus Alexander:** Writing – review & editing, Writing – original draft, Visualization, Validation, Software, Project administration, Methodology, Investigation, Formal analysis, Data curation, Conceptualization.

Declaration of Competing Interest

The authors declare that they have no known competing financial interests or personal relationships that could have appeared to influence the work reported in this paper.

Acknowledgements

The authors thank Štefan Stanko and Jürgen E. K. Schawe from ETH Zurich for fruitful discussions. The in-situ XRD tomography experiments were carried out with the support of ESRF (beamline ID11, proposal HC-4089). The authors are also grateful to Carlotta Giacobbe from ESRF and Florian Spieckermann from Montanuniversität Leoben for their help with the measurements at ID11. The SAXS experiments were carried out with the support of DESY (beamline P62, proposal I-20210311 EC). The

calculations related to the reconstruction of the XRD-nCT data were run on the Euler cluster of ETH Zurich. The authors gratefully acknowledge the support by an ETH Research Grant (ETH-47 17–1) and the ETH+ initiative within the framework of SynMatLab (Laboratory for Multiscale Materials Synthesis and Hands-On Education).

Appendix A. Supporting information

Supplementary data associated with this article can be found in the online version at doi:10.1016/j.jallcom.2025.180013.

Data availability

The nCT-XRD datasets of this study are made publicly available by ESRF: "Time-resolved spatial local atomic fluctuations related to the Invar effect in metallic glasses studied by XRD-nCT", DOI 10.15151/ESRF-DC-1661690354. The calibrated datasets are available in the ETH Research collection, Datasets to "The origin of magneto-structural coupling in Fe-based bulk metallic glasses", DOI 10.3929/ethz-b-000613779.

References

[1] C.-É. Guillaume, Invar and elinvar, Nobel Lect. Phys. (1920) 444–473. ⟨https://www.nobelprize.org/prizes/physics/1920/guillaume/lecture/⟩.
[2] C.-É . Guillaume, Invar and its applications, Nature 71 (1904) 134–139, https://doi.org/10.1038/071134a0.
[3] S.H. Lohaus, M. Heine, P. Guzman, C.M. Bernal-Choban, C.N. Saunders, G. Shen, O. Hellman, D. Broido, B. Fultz, A thermodynamic explanation of the Invar effect, Nat. Phys. 19 (2023) 1642–1648, https://doi.org/10.1038/s41567-023-02142-z.
[4] M. van Schilfgaarde, I.A. Abrikosov, B. Johansson, Origin of the Invar effect in iron–nickel alloys, Nature 400 (1999) 46–49, https://doi.org/10.1038/21848.
[5] Q. Hu, J.M. Wang, Y.H. Yan, S. Guo, S.S. Chen, D.P. Lu, J.Z. Zou, X.R. Zeng, Invar effect of Fe-based bulk metallic glasses, Intermetallics 93 (2018) 318–322, https://doi.org/10.1016/j.intermet.2017.10.012.
[6] K.H.J. Buschow, E.P. Wohlfarth, Handbook of Magnetic Materials, Elsevier Science Publisher B.V, 1990.
[7] E.F. Wassermann, The Invar problem, J. Magn. Magn. Mater. 100 (1991) 346–362, https://doi.org/10.1016/0304-8853(91)90828-X.
[8] Z. Rao, D. Ponge, F. Körmann, Y. Ikeda, O. Schneeweiss, M. Friák, J. Neugebauer, D. Raabe, Z. Li, Invar effects in FeNiCo medium entropy alloys: From an Invar treasure map to alloy design, Intermetallics 111 (2019) 106520, https://doi.org/10.1016/j.intermet.2019.106520.
[9] A. Firlus, M. Stoica, S. Michalik, R.E. Schäublin, J.F. Löffler, Atomic structure evolution related to the Invar effect in Fe-based bulk metallic glasses, Nat. Commun. 13 (2022) 1082, https://doi.org/10.1038/s41467-022-28650-9.
[10] A. Firlus, M. Stoica, G.B.M. Vaughan, R.E. Schäublin, J.F. Löffler, The nature of the atomic-scale Invar effect in Fe-based bulk metallic glasses, Mater. Today Nano. 24 (2023) 100394, https://doi.org/10.1016/j.mtnano.2023.100394.
[11] K. Fukamichi, H. Hiroyoshi, M. Kikuchi, T. Masumoto, Invar effects on some iron-base amorphous alloys, J. Magn. Magn. Mater. 10 (1979) 294–299, https://doi.org/10.1016/0304-8853(79)90194-X.
[12] D.H. Kim, J.M. Park, D.H. Kim, W.T. Kim, Development of quaternary Fe-B-Y-Nb bulk glassy alloys with high glass-forming ability, J. Mater. Res. 22 (2007) 471–477, https://doi.org/10.1557/jmr.2007.0057.
[13] Z. Han, J. Zhang, Y. Li, Quaternary Fe-based bulk metallic glasses with a diameter of 5mm, Intermetallics 15 (2007) 1447–1452, https://doi.org/10.1016/j.intermet.2007.05.007.
[14] S. Haas, X. Sun, A.L.C. Conceição, J. Horbach, S. Pfeffer, The new small-angle X-ray scattering beamline for materials research at PETRA III: SAXSMAT beamline P62, J. Synchrotron Radiat. 30 (2023) 1156–1167, https://doi.org/10.1107/S1600577523008603.
[15] Q. Hu, H.C. Sheng, M.W. Fu, X.R. Zeng, Influence of melt temperature on the Invar effect in $(Fe_{71.2}B_{24}Y_{4.8})_{96}Nb_4$ bulk metallic glass, J. Mater. Sci. 49 (2014) 6900–6906, https://doi.org/10.1007/s10853-014-8392-z.
[16] Q. Hu, X.R. Zeng, M.W. Fu, Invar effects of $(Fe_{71.2}B_{24}Y_{4.8})_{96}Nb_4$ alloy in different structural states, Appl. Phys. Lett. 97 (2010) 221907, https://doi.org/10.1063/1.3524199.
[17] I.-R. Lu, G. Görler, H.-J. Fecht, R. Willnecker, Investigation of specific heat and thermal expansion in the glass-transition regime of Pd-based metallic glasses, J. Non Cryst. Solids 274 (2000) 294–300, https://doi.org/10.1016/S0022-3093(00)00220-9.
[18] T. Lu, S.L. Liu, Y.H. Sun, Z.Y. Liu, W. Wang, M. Pan, 1.7 Times thermal expansion from glass to liquid, Acta Mater. 242 (2023) 118450, https://doi.org/10.1016/j.actamat.2022.118450.
[19] M. Stoica, B. Sarac, F. Spieckermann, J. Wright, C. Gammer, J. Han, P.F. Gostin, J. Eckert, J.F. Löffler, X-ray diffraction computed nanotomography applied to solve the structure of hierarchically phase-separated metallic glass, ACS Nano 15 (2021) 2386–2398, https://doi.org/10.1021/acsnano.0c04851.
[20] S. Scudino, J. Han, R.N. Shahid, D. Bieberstein, T. Gemming, J. Wright, Strain fields as local probe for X-ray diffraction tomography: non-destructive reconstruction of shear band paths in metallic glasses, J. Alloy. Compd. 958 (2023) 170484, https://doi.org/10.1016/j.jallcom.2023.170484.
[21] A.M. Korsunsky, N. Baimpas, X. Song, J. Belnoue, F. Hofmann, B. Abbey, M. Xie, J. Andrieux, T. Buslaps, T.K. Neo, Strain tomography of polycrystalline zirconia dental prostheses by synchrotron X-ray diffraction, Acta Mater. 59 (2011) 2501–2513, https://doi.org/10.1016/j.actamat.2010.12.054.
[22] V.L. Moruzzi, P.M. Marcus, Magnetism in bcc 3 d transition metals: onset and approach to the Hund's-rule limit, Phys. Rev. B. 38 (1988) 1613–1620, https://doi.org/10.1103/PhysRevB.38.1613.
[23] C. Suryanarayana, A. Inoue, Iron-based bulk metallic glasses, Int. Mater. Rev. 58 (2013) 131–166, https://doi.org/10.1179/1743280412Y.0000000007.
[24] S.J. Poon, G.J. Shiflet, F.Q. Guo, V. Ponnambalam, Glass formability of ferrous- and aluminum-based structural metallic alloys, J. Non Cryst. Solids 317 (2003) 1–9, https://doi.org/10.1016/S0022-3093(02)02000-8.